Kinetic Monte Carlo simulations of Pd deposition and island growth on MgO(100)

Lijun Xu [a], Charles T. Campbell [b], Hannes Jónsson [c], Graeme Henkelman [a,*]

[a] *Department of Chemistry and Biochemistry, University of Texas at Austin, Austin, TX 78712-0165, United States*
[b] *Department of Chemistry 351700, University of Washington, Seattle, WA 98195-1700, United States*
[c] *Faculty of Science, VR-II, University of Iceland, 107 Reykjavík, Iceland*

Abstract

The deposition and ripening of Pd atoms on the MgO(100) surface are modeled using kinetic Monte Carlo simulations. The density of Pd islands is obtained by simulating the deposition of 0.1 ML in 3 min. Two sets of kinetic parameters are tested and compared with experiment over a 200–800 K temperature range. One model is based upon parameters obtained by fitting rate equations to experimental data and assuming the Pd monomer is the only diffusing species. The other is based upon transition rates obtained from density functional theory calculations which show that small Pd clusters are also mobile. In both models, oxygen vacancy defects on the MgO surface provide strong traps for Pd monomers and serve as nucleation sites for islands. Kinetic Monte Carlo simulations show that both models reproduce the experimentally observed island density versus temperature, despite large differences in the energetics and different diffusion mechanisms. The low temperature Pd island formation at defects is attributed to fast monomer diffusion to defects in the rate-equation-based model, whereas in the DFT-based model, small clusters form already on terraces and diffuse to defects. In the DFT-based model, the strong dimer and trimer binding energies at charged oxygen vacancy defects prevent island ripening below the experimentally observed onset temperature of 600 K.
© 2007 Elsevier B.V. All rights reserved.

1. Introduction

Metal films and particles supported on oxide surfaces are widely used in material science and for heterogeneous catalysis [1–6]. Model catalysts consisting of vapor-deposited metals on single-crystalline oxide surfaces are studied in order to understand generic questions such as how metal nanoparticles grow and ripen, and which factors contribute to their catalytic activity. The Pd/MgO(100) system, in particular, has been extensively studied as a prototypical metal/oxide system [2]. One of the motivations for understanding the microscopic details of Pd particle growth and sintering dynamics is to determine how to design a system with metal

particles on an oxide surface that resists sintering [7–13]. In this study, we build upon the many experimental and theoretical studies that have been devoted to understanding Pd particle growth, ripening and energetics on MgO(100) [2,14–19]. Our main goals are to connect the microscopic transition mechanisms with ripening dynamics on experimental time scales through the use of kinetic Monte Carlo simulations, and to explore the implications of recent DFT calculations of Pd cluster energies and migration rates on perfect and defective MgO(100) [20–23].

1.1. Atomic force microscopy experiments

A significant step forward in the understanding of Pd ripening dynamics on MgO(100) was made in the experimental work of Brune and coworkers [24,25], who used

---

* Corresponding author.
E-mail address: henkelman@mail.utexas.edu (G. Henkelman).

atomic force microscopy (AFM) to measure the Pd island density as a function of temperature, and the theoretical work of Venables and coworkers, who developed a microscopic model with only a few adjustable parameters which reproduces the experimental measurements [14,17,25–27]. The experiments start with an Ar-cleaved MgO(100) surface, upon which 0.1 ML of Pd atoms are deposited in the course of 3 min. After deposition, the Pd islands are viewed with *in situ* atomic force microscopy (AFM) to determine the island density. This procedure is repeated for temperatures between 200 and 800 K. What is initially striking about the results (see Fig. 2) is that the island density is constant over a wide range of temperature between 200 and 600 K. This plateau is attributed to defects on the surface which nucleate the formation of Pd islands. The plateau island density of $2.8 \times 10^{12} \, \text{cm}^{-1}$ is consistent with the observed defect density of 10^{12}–10^{13} defects/cm^2 on an UHV-cleaved MgO(100) surface [28]. Above 600 K, ripening is activate and the island density drops.

1.2. Mean field modeling

The Pd island density data have been modeled by Haas et al. [25] through the construction of a set of coupled differential equations for the concentration of each Pd$_n$ cluster size. This model is based upon a simple set of microscopic mechanisms and corresponding energetics. Pd monomers are assumed to be the only diffusing species, and are described by a uniform (mean field) concentration on the terrace. This concentration is determined from the balance of atoms being deposited onto the surface, the evaporation of monomers from existing clusters, and the attachment of these free monomers to islands or defects. An upper limit on the monomer diffusion barrier is set at 0.2 eV, so that a deposited monomer is able to reach a defect at the lowest temperatures tested (200 K), before meeting another monomer and nucleating a new island on the terrace. With this fast monomer diffusion, the island density is constant and equal to the defect density from 600 K down to 200 K, in agreement with experiment.

Above 600 K, ripening is inferred from a decrease in the Pd island density. In the mean field model, ripening occurs when monomers detach from clusters, overcoming the dimer binding energy. This can be the dissociation of a dimer into two monomers, or the dissociation of a monomer from a larger cluster. This dimer binding energy is fit to a value of 1.2 eV, in order to match the observed island density decrease at the onset of ripening.[1]

---

[1] Note that it is actually the *barrier* for dimer dissociation which determines the ripening temperature. The dissociation process is assumed to have a reverse barrier equal to the monomer diffusion barrier (0.2 eV), giving an overall dimer dissociation activation energy of 1.4 eV. This barrier is consistent with a process that is activated at 600 K: assuming a standard prefactor of $10^{12} \, \text{s}^{-1}$, transition state theory predicts a lifetime of 0.1 s for the dimer at 600 K, which is the time scale on which a Pd atom is deposited per defect site.

With just a few adjustable parameters the mean field model fits the experimental island density data [25,17]. The agreement is compelling, but one can still worry that the fit is not unique. That is, if a different underlying model is assumed, the rate parameters could have significantly different values, and agreement with experiment reached for different reasons. In this model, two important underlying assumptions are that (a) Pd monomers are the only mobile species on the terrace and (b) small clusters form two-dimensional epitaxial islands, or more precisely, that the binding energy of Pd atoms in a cluster can be written as the pairwise sum of lateral bonds which are consistent with two-dimensional island growth.

It is important to emphasize that these assumptions are not a limitation of the modeling approach. The rate equations can be modified to include more complicated diffusion mechanisms, three-dimensional clusters, and many other factors that might be important for the dynamics. This approach (on its own), however, is only tractable and convincing if the experimental data can be fit using a simple model with a few adjustable parameters.

1.3. Density functional theory calculations

Density functional theory (DFT) calculations have also been used to investigate the energy landscape of Pd on MgO, and show that the structure and kinetics of small Pd clusters are more complex than previously assumed. Specifically, small Pd clusters of three or more atoms energetically favor three-dimensional structures [20–22,29], and these clusters form spontaneously [22,29]. Another surprise from DFT calculations is that the monomer is not the only mobile species on the MgO surface. Small clusters, at least up to the tetramer, are also mobile [22,23]. In fact, it has been calculated that the tetramer diffuses faster than all smaller clusters (including the monomer) for temperatures above 200 K [22]. This cluster mobility could play an important role for the ripening kinetics of Pd on MgO [23], as it does for Au on Al$_2$O$_3$ [30].

The nature of defects on MgO(100) and the binding of Pd clusters to these defects is also important for understanding the ripening dynamics of Pd clusters. [28,31, 20,32,21,33]. The neutral oxygen vacancy (*F*-center) binds a Pd monomer very strongly, with an energy of 2.6 eV [29]. When two Pd atoms bind at the *F*-center, however, the second has a lower binding energy of 0.56 eV. This dimer binding energy is weaker than the 1.2 eV needed to reproduce the ripening temperature in the mean field model. Such a weak dimer binding energy is not specific to Pd; Bogicevic and Jennison [34] have calculated that the Pt dimer is unstable at the *F*-center on MgO. If dimer dissociation at the *F*-center is the correct mechanism of ripening, there is a discrepancy between the energy of this process found with DFT (0.56 eV) and that required by the rate equation model to match experiment (1.2 eV).

Details of the DFT calculations used in this paper are given in Ref. [29]. The calculations were done with periodic

slabs using a plane wave basis set and the Perdew-Wang (PW-91) gradient corrected (GGA) functional. The specifics of these calculations are not of primary importance in this work. The main results from the DFT calculations, such as the weak dimer binding energy at *F*-centers, are insensitive to the computational details. Giordano et al. have shown this by comparing periodic calculations (essentially the same as ours) with cluster-based DFT calculations using local basis sets and a hybrid B3LYP functional [20]. In the case of the dimer at *F*-centers, the B3LYP dimer binding energy is somewhat lower (0.39 eV) than the PW-91 calculations (0.56 eV). Both values, however, are significantly different from the fitted values in the rate equations (1.2 eV). The average difference in Pd binding at various sites on MgO, between periodic PW-91 and B3LYP cluster calculations, was found to be on the order of 0.1 eV [20]. The DFT energies presented here should be assumed to have uncertainties on this order.

Recently, Giordano et al. [20,32,21] have suggested that the inconsistency between DFT and the rate model can be resolved if the defects on MgO are not neutral *F*-centers. Their DFT calculations show a stronger dimer binding energy at the F^+-center (0.91 eV) and neutral di-vacancy (1.50 eV) defects. Furthermore, it was shown that three-dimensional clusters are energetically favorable at these defects. Since these calculations were done, Venables et al. have been able to adjust the mean field model to accommodate the DFT binding energetics of three-dimensional clusters at defects without substantially altering the assumptions or fitting parameters [27].

1.4. First principles kinetic modeling

The rate equation based model starts with a set of assumptions about the important diffusion mechanisms. Unknown rates are then fit to reach agreement with experiment using the minimum number of elementary steps that reproduce all observations. If agreement cannot be reached, or if more data is provided (such as from DFT calculations) the underlying assumptions and/or diffusion mechanisms may need to be changed.

In this work, we take a different approach. Our starting point is the use of DFT calculations to map out as much of the energy landscape as we can for Pd clusters on MgO, by building up a set of cluster binding energies and diffusion barriers. In this approach, we include as many elementary steps as possible and use their propagation in time to determine which of these steps are kinetically relevant. Unbiased saddle point searches [35–38] are used to find unexpected diffusion mechanisms, such as the mobility of small Pd clusters [22,29]. Reaction rates, *k*, are derived from energy barriers, ΔE, and prefactors, *v*, using the harmonic form of transition state theory,

$$k = v e^{-\Delta E/kT}. \tag{1}$$

For many diffusion mechanisms, the prefactor has been calculated explicitly,

$$v = \frac{\Pi_i^{3N} v_i^{\text{init}}}{\Pi_i^{3N-1} v_i^{\ddagger}}, \tag{2}$$

as the ratio of harmonic modes in the initial state v_i^{init} and the stable modes at the saddle point $v_i^{\ddagger}$. For those reactions in which the prefactor was not calculated, a standard value of 10^{12} s^{-1} was assumed.

We then use these rates in a kinetic Monte Carlo simulation, and compare the calculated Pd island density with experiment. In this way, we avoid fitting kinetic parameters, and minimize our assumptions about the structure and diffusion mechanisms of Pd clusters.

2. Simulation methodology

The method we use to connect our DFT calculations with experiment is kinetic Monte Carlo (KMC) [39–41]. KMC is an efficient tool for modeling a sequence of thermally activated rare events based upon rates from a potential energy surface [42,43]. In our simulations, we use DFT calculations to provide the possible reactions and corresponding rates. KMC is a complementary method to the mean field rate equation approach [17], and the two agree when the underlying physics is the same and the mean field approximation is valid [24]. KMC is different, however, in that each activated event is followed (such as monomer diffusion hopping), as well as the position of each Pd atom in time. This additional microscopic detail makes it easier to include many diffusion processes into the model, and learn which are important from the dynamics. The spatial resolution in KMC also relaxes the mean field approximation; spatially correlated events such as cluster–cluster interactions and the configurational entropy of clusters are automatically taken into account.

KMC allows us to bridge the time scale gap between fast diffusion events (nanoseconds) and the slower time scale of deposition events (seconds). To reach the experimental time scales, we have to simulate many (10^6–10^9) microscopic diffusion events. A table of all possible kinetic events are required for every configuration that the system visits. Each event is assigned a probability proportional to its rate, and one chosen with the correct statistical weight using a random number generator. The atoms in the system are then moved to the final state of the chosen event, and the simulation clock is incremented by a time selected at random from a Poisson distribution with a mean (first escape) time equal to the inverse of the sum of the rates.

Two sets of reaction mechanisms and rates are investigated. First, those of the Haas et al. mean field model [25] are tested so that our KMC simulations can be directly compared with the rate equation approach. In this model, the Pd monomer is the only mobile species, and Pd islands are assumed to be epitaxial (two-dimensional). The second set are taken from DFT calculations of Pd clusters on MgO(1 0 0) [29]. In these simulations, small clusters spontaneously form three-dimensional structures which are mobile on the MgO surface.

3. Results

3.1. KMC based upon rate equation parameters

To compare our KMC simulations with the rate equation model of Haas et al., we have attempted to match their assumptions (see Fig. 1) and the experimental conditions as closely as possible [25]. The following list details this mapping.

1. *The MgO(100)* surface is represented by a 100×100 square grid of oxygen sites.
2. *Point defects* have a density of $2.8 \times 10^{12}\,\mathrm{cm^{-2}}$, which corresponds to 0.25% of surface oxygen sites. At the start of the simulation, 25 of the 10,000 grid sites are randomly chosen to be defect sites (excluding cases with neighboring defects).
3. *Pd deposition* is at a rate of 3.2×10^{-2} ML/min until a coverage of 0.1 ML is reached [1 ML $= 1.13 \times 10^{15}\,\mathrm{cm^{-2}}$]. In the KMC calculations, this corresponds to a Pd deposition rate of $5.33\,\mathrm{s^{-1}}$, so that 1000 Pd atoms are deposited randomly onto the surface in a simulated time of 190 s.
4. *Pd monomers* are assumed to be the only diffusing species, hopping on the terrace with a barrier of 0.2 eV. The same diffusion barrier is used for the KMC simulation, with a standard prefactor of $10^{12}\,\mathrm{s^{-1}}$.
5. *Pd dimers* dissociate by overcoming a binding energy of 1.2 eV and a barrier of 1.4 eV. This barrier contains the 1.2 eV dimer binding energy plus the 0.2 eV monomer diffusion barrier. In this way, detailed balance is maintained for dimer formation and dissociation. The dimer binding energy is taken as a pairwise additive interaction for Pd atoms with more than one neighbor. A Pd atom with two nearest neighbors, for example, dissociates from both neighbors with a barrier of 2.6 eV, $(2 \times 1.2 + 0.2\,\mathrm{eV})$.
6. *Pd islands* are assumed to be two-dimensional on the terrace. This condition is enforced in the KMC simulation by only allowing one Pd atom per O site.
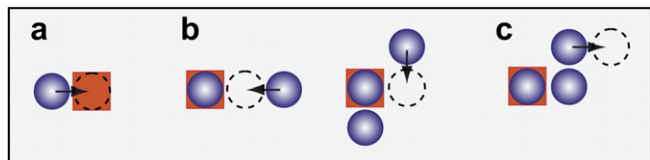

Fig. 1. Examples of transitions included in the mean-field, rate equation based model of Pd island growth on MgO(100). Monomers (purple circles), which are the only mobile species, bind strongly when they encounter defect sites (red squares). Arrows show possible transitions, including (a) trapping at a defect site, (b) binding to other Pd atoms, and (c) dissociation from a cluster. (For interpretation of the references to colour in this figure legend, the reader is referred to the web version of this article.)
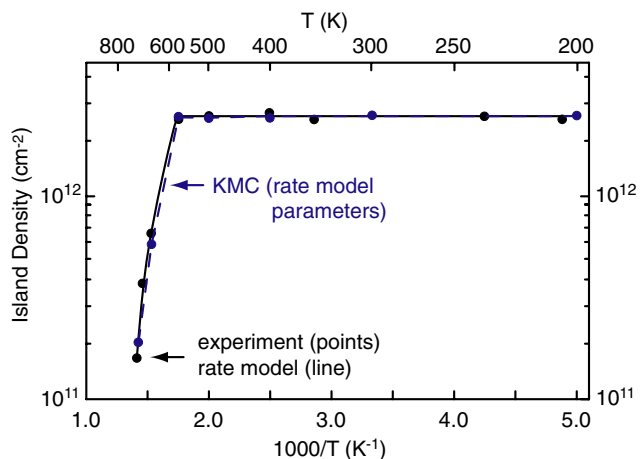

Fig. 2. Comparison of experimentally observed Pd island densities after deposition of 0.1 ML (black points), with those calculated from a rate equation model [data from Ref. [25]] (solid line) and corresponding KMC simulation data (blue points). The agreement shows that our KMC simulations correctly reproduce the rate equation models, which have in turn been fit to match experiments. (For interpretation of the references to colour in this figure legend, the reader is referred to the web version of this article.)

7. *Pd trapping* energy at a defect site is 1.5 eV. The energy barrier for a monomer to leave a defect site onto the terrace is taken to be 1.7 eV (including the 0.2 eV monomer diffusion barrier).
8. *Pd desorption* takes place only at elevated temperatures, and is still slow compared to the other processes at 600 K. Since, we are primarily interested in low temperature island formation and the onset of ripening which occurs experimentally at 600 K, we have not included desorption in our KMC simulations.

Fig. 2 shows the calculated island density from these KMC simulations, and the close agreement with the experiments and mean field model of Haas et al. The island shapes formed in the KMC simulations are shown in Fig. 3. The islands change from dendritic at low temperature to compact at 600 K. This detail is not represented in the rate equation model, but also does not affect the island density in this particular system. Pd islands form exclusively around defect sites; no additional islands form on the terrace. The onset of island ripening occurs at 600 K, which can be seen from the drop in island density (Fig. 2) and the increase in the size of the largest Pd islands (Fig. 3). For all but the highest temperatures, O vacancies remain filled by trapped Pd monomers. These monomers are not counted as islands in the KMC or mean-field models, which is appropriate for comparison with the AFM experiments.

3.2. KMC simulations from first principles energetics

DFT calculations show that the mechanisms of Pd cluster growth and ripening [22,29] are somewhat different
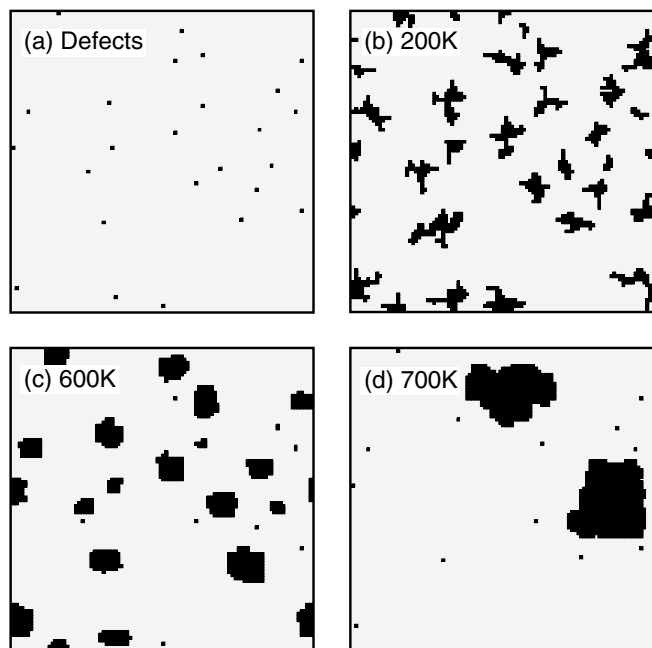
Fig. 3. KMC simulations of Pd island growth after deposition of 0.1 ML, using parameters taken from a mean-field, rate equation based model. Defect sites are shown in (a). Dots and dark regions (b–d) are Pd monomers and larger islands, respectively. Monomer islands are not considered when calculating the island density. [Note: the simulations include periodic boundary conditions.]

from what is assumed in the rate equation model [24,25]. Fig. 4a shows several such diffusion events for Pd clusters on the terrace, calculated from DFT. Clusters, larger than the dimer, spontaneously form 3D structures, and clusters up to the tetramer are mobile. Small Pd_{n-1} clusters can also dissociate from a Pd_n cluster at a defect (see Fig. 4b) leaving behind a monomer-defect complex. These monomers are bound irreversibly to the defects in the relevant temperature range (<800 K). Larger clusters form strongly bound 3D structures (e.g. Fig. 4e) which are stable for all temperatures of interest.
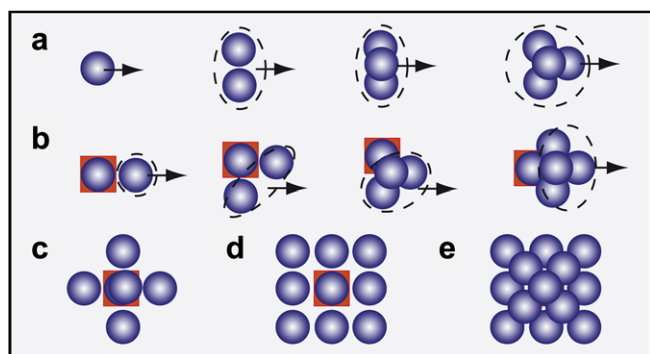

Fig. 4. DFT calculations [29] show that (a) Pd clusters, up to the tetramer, are mobile, and (b) these clusters can dissociate from monomer-bound *F*-center complexes. Larger clusters, which nucleate at defect sites (c–e), are highly stable in a square pyramidal structure.

In the KMC simulations, the structures found with DFT [21,29] are mapped onto a square simulation grid. Our mapping of the most stable clusters is shown in Fig. 5. Each square represents an oxygen site, and the value indicates the number of Pd atoms in the cluster. The monomer and dimer structures have one Pd atom on each site. The trimer on the terrace, however, is a vertical structure (see Fig. 4a) for which three atoms occupy two sites. When bound to an oxygen vacancy defect, the trimer takes a 2D form and occupies an additional site. The tetramer takes a 3D tetrahedral form, occupying three O sites, all sharing a common Mg site. The tetramer can easily rotate about this Mg site. We do not explicitly model this fast rotation in our KMC simulation; to represent this rotation, the tetramer is assumed to occupy all four O sites around the Mg. In a similar way, the pentamer forms a square pyramidal structure, occupying four O sites, and the hexamer occupies five sites. The atomic detail of larger clusters is not accurately reproduced in the KMC simulations. These clusters are assumed to have pyramidal structures with square footprints [2,19], similar to those observed in experiment [44], and predicted by an empirical potential [45]. Clusters with 7–14 atoms occupy a 3×3 square of sites, 15–30 atoms a 4×4 square, and so on. The actual number of atoms in the cluster is recorded on the simulation grid. If a 14 atom cluster, for example, gains an

Fig. 5. Pd islands are represented in the KMC simulations on a square grid. Each grid point is an oxygen site, or an oxygen vacancy defect site (neutral *F*-center, shown darker in the figure). The minimum energy structure of each cluster (calculated from DFT) is mapped onto the grid. The trimer, for example, has a vertical structure and occupies two lattice sites. The pentamer takes the form of a square pyramid and occupies four lattice sites. Clusters with more than six atoms are represented as square based pyramids. Those with 7–14 atoms occupy a 3×3 area, and those with 15–30 atoms a 4×4 area. The maximum number of atoms for each square is the number which fills a regular square pyramidal particle.

Table 1
Kinetic parameters for small Pd$_n$ ($n = 1$–5) clusters on the terrace and at oxygen vacancies (neutral F-centers) based on DFT calculations

Event	Barrier (eV)	Prefactor (s^{-1})[a]
1(a) Monomer hop, terrace	0.34	7.35×10^{11}
2(a) Dimer hop (a), terrace	0.43	4.16×10^{10}
2(b) Dimer hop (b), terrace	0.11	2.01×10^{12}
2(c) Dimer slide, terrace	0.60	3.59×10^{10}
2(d) Dimer hop/dissociation, terrace	0.56	3.0×10^{14}
2(e) Dimer dissociation, terrace	0.84	4.14×10^{11}
2(f) Dimer dissociation, F-center	0.88	10^{12}
2(g) Dimer dissociation, F-center	0.70	10^{12}
2(h) Dimer contraction, F-center	0.11	10^{12}
3(a) Trimer hop (a), terrace	0.48	5.37×10^{10}
3(b) Trimer hop (b), terrace	0.21	4.36×10^{12}
3(c) Trimer slide, terrace	0.94	3.38×10^{11}
3(d) Trimer dissociation, terrace	1.38[b]	10^{12}
3(e) Trimer dissociation, F-center (1)	1.23[b]	10^{12}
3(f) Trimer dissociation, F-center (2)	1.09[b]	10^{12}
4(a) Tetramer hop, terrace	0.41	1.28×10^{14}
4(b) Tetramer dissociation, terrace	2.05[b]	10^{12}
4(c) Tetramer dissociation, F-center (1)	1.62[b]	10^{12}
4(d) Tetramer dissociation, F-center (2)	1.73[b]	10^{12}
5(a) Pentamer dissociation, terrace	1.72[b]	10^{12}
5(b) Pentamer dissociation, F-center (1)	1.23[b]	10^{12}
5(c) Pentamer dissociation, F-center (2)	1.73[b]	10^{12}

Dimers and trimers diffuse via two sequential hopping steps, indicated by (a) and (b). Trimers, tetramers and pentamers can dissociate from F-centers either by (1) detaching a cluster with one less atom and leaving a monomer behind on the defect, or by (2) detaching a monomer, leaving behind the smaller cluster bound to the defect. Detailed information about these mechanisms can be found in Refs. [22,29,21].
[a] A value of 10^{12} s^{-1} was assumed for any mechanism in which a prefactor was not explicitly calculated.
[b] The dissociation barrier was estimated from the difference between initial and final state energy, plus the diffusion barrier of the dissociated species on the terrace.

additional atom, the new cluster is marked with the cluster number 15 in each grid point within the 4×4 grid of occupied sites. With this marking system, each cluster size and structure is uniquely indicated on the KMC simulation grid.

To simulate Pd growth and ripening dynamics using KMC, a list of all kinetic events is needed, that are accessible in the simulation time (3 min) and temperature range (200–800 K). The event table and corresponding rates are calculated from the DFT energy barriers and prefactors listed in Table 1, using the Arrhenius equation (Eq. (1)). Fig. 6 shows how the diffusion mechanisms are mapped onto the simulation grid. At each KMC step, a process is chosen at random from a list of all possible reaction mechanisms, including the Pd deposition event, which occurs with the experimental deposition rate of 5.33 s^{-1} (for the simulation surface containing 10,000 sites). If the deposition event is chosen, a Pd atom is added to an unoccupied site in the simulation grid. The approximation that no deposited atom lands on an existing island simplifies the deposition algorithm without significantly biasing the simulation since the experimental data is for low Pd coverages up to 0.1 ML. One final change to the standard KMC algorithm is required; after each KMC step, the surface is scanned to see if any new islands were formed. For example, if a monomer diffuses next to another monomer, the two sites are reassigned as a dimer. Apart from the difference between the DFT energy landscape and that of the
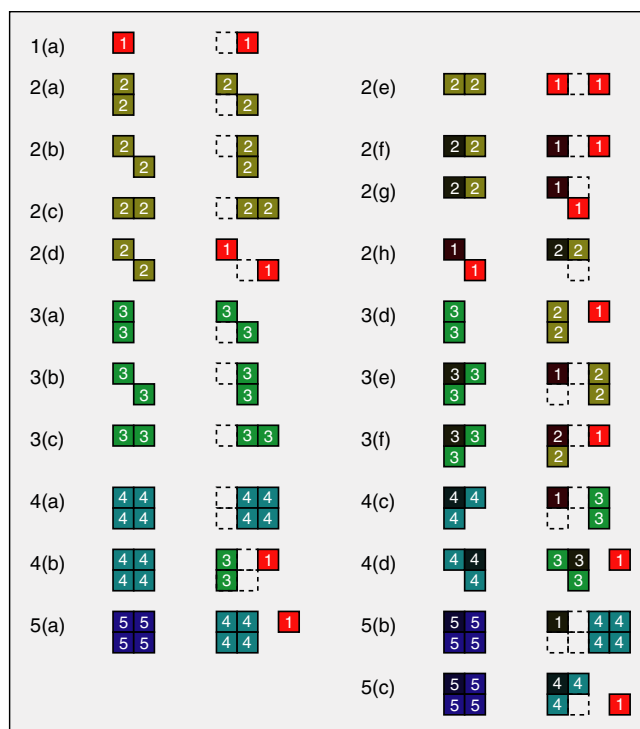

Fig. 6. Kinetic events from Table 1 are mapped onto the simulation grid. For each mechanisms, the initial and final states are shown. In the final state, dashed outlines indicate sites that were occupied in the initial state.

monomer diffusion based rate equation model, the KMC simulation parameters, such as simulation size, deposition rate, temperature range, are the same as described in Section 3.1 to match the experiments of Haas et al. [25].

3.3. Cluster mobility at low temperature

The KMC simulation of island density as a function of temperature are plotted in Fig. 7. Both the rate equation fitted parameters and those based on our DFT calculations predict that the island density is equal to the defect density at low temperatures, indicating that Pd is able to diffuse to defect site before forming immobile clusters. There is, however, an important difference between the two models. The rate equation model assumes that the monomer is the only diffusing species, and the fitted value of the monomer diffusion barrier is necessarily low (0.2 eV) so that monomers can rapidly diffuse to defect sites before nucleating a cluster on the terrace. The DFT calculations predict a higher monomer diffusion barrier of 0.34 eV, so that at 200 K, clusters do nucleate on the terrace. Small clusters (trimers and tetramers) are, however, highly mobile, so they diffuse and find defects before additional monomers cause them to grow into larger, immobile clusters [22,23]. Fig. 8 shows a representative example of this agglomeration mechanism seen in a KMC simulation at 200 K. In Fig. 8b, a dimer has formed in the circled region. Several seconds later, a diffusing monomer merges with the dimer, forming a trimer (c). Soon after, another monomer joins the cluster to form a rapidly diffusing tetramer, and in a fraction of a second (d) the cluster diffuses and agglomerates with an immobile cluster at a defect site. This ripening mechanism is fairly common at 200 K. In the simulation shown in Fig. 8, seven clusters nucleate on the terrace and diffuse to islands at de-

Fig. 8. KMC simulation snapshots of Pd island growth on MgO(100) surface with kinetic parameters from DFT calculations. The color and size of the clusters are as shown in Fig. 5. In each figure there is one monomer (red) on the terrace. All clusters are bound at defect sites, except for those in the circled regions (in b and c). At 55 s, a dimer forms in the circled region on the terrace (b), diffuses and merges with a monomer to form a trimer (c), before it encounters one more monomer to become a tetramer on the terrace (not shown). The tetramer diffuses rapidly at 200 K so that very soon afterwards (d) the tetramer diffuses out of the circled region and agglomerates with an island at a defect site, below it and to the left. (For interpretation of the references to colour in this figure legend, the reader is referred to the web version of this article.)
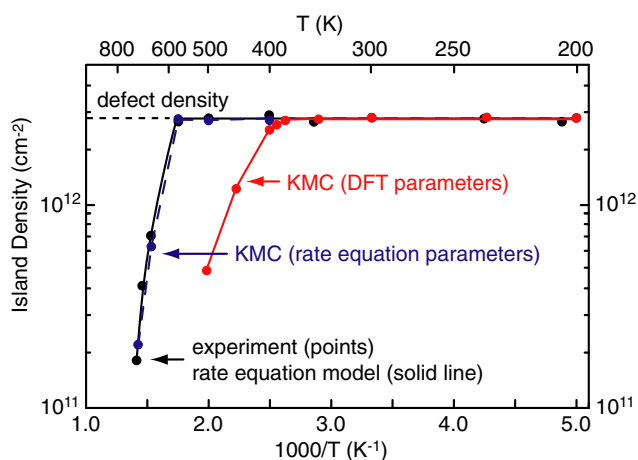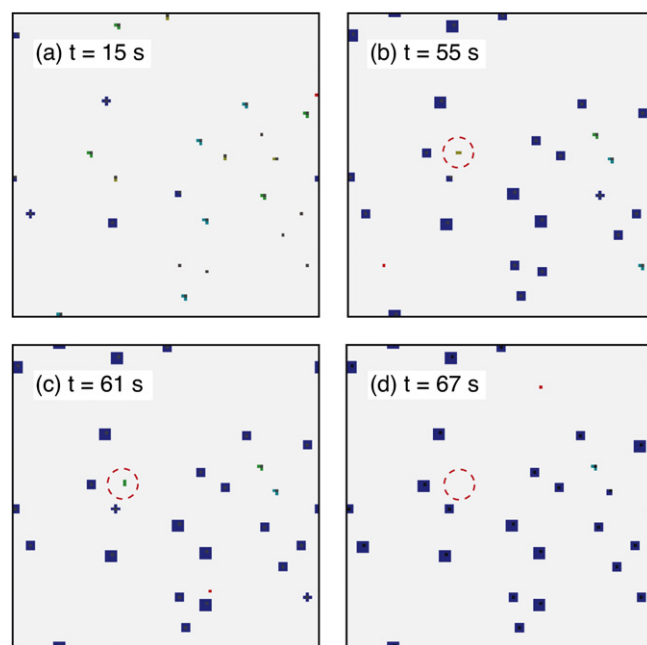

Fig. 7. KMC simulations using parameters calculated from DFT show that the island density is the same as the defect density at low temperature, matching the rate equation model (and experiment). This is due to a high monomer diffusivity in the later, and high cluster mobility in the former. The onset of ripening is predicted at 380 K, significantly lower than the rate equation value of 600 K, due to the different values of the dimer binding energy at defects.

fect sites. Had these clusters been immobile, as assumed in the rate equation model, the island density would have been overestimated by 30% at 200 K compared to the results from these DFT-based energetics.

3.4. Dimer stability at high temperature

The KMC simulated island density based on DFT parameters (see Fig. 7) has a lower ripening temperature (380 K) as compared with the rate equation model and experiment (590 K). The reason for this is that DFT predicts a lower dimer dissociation barrier (0.70 eV) than the fit of the rate equation model to these experiments (1.4 eV). The importance of the dimer dissociation barrier on the ripening temperature can be understood from the following stages of growth observed at elevated temperatures (300–800 K):

1. The first deposited Pd monomers rapidly diffuse until they find a defect. If the defect is unoccupied, the monomer binds irreversibly.
2. As defects become occupied, deposited monomers diffuse to the defects to form dimers. If the dimer dissociation mechanism is not thermally active, the dimers are

immobile and clusters nucleate. If the dissociation mechanism is active, monomers are able to dissociate and diffuse to other monomer-bound defect sites.

3. Once a small cluster forms at a defect site, this cluster strongly binds any monomer that diffuses to it. If the dimer dissociation process is active, monomers can diffuse from far away. In this way, monomers will add to the growth of established clusters at defects, without nucleating additional clusters at the monomer-saturated defects.

The ripening temperature can be estimated from this simple picture as the temperature T_{rip} at which the rate of dimer dissociation at a defect is equal to the deposition rate per defect site ($R_{dep} = 0.2$ s^{-1})

$$R_{dep} = v e^{-\Delta E/kT_{rip}}, \tag{3}$$

where ΔE and v are the barrier and prefactor for dimer dissociation. With the DFT barrier of 0.70 eV and a prefactor of 10^{12} s^{-1}, this ripening temperature is 280 K. The rate equation model has a dimer dissociation barrier of 1.4 eV and a corresponding ripening temperature of 560 K. These temperatures correspond to the points at which the island density starts deviating from the defect density in the KMC simulations (see Fig. 7).

Eq. 3 also provides a relationship between an uncertainty in the DFT energetics and the corresponding ripening temperature. The ripening barrier, ΔE, and the ripening temperature, T_{rip}, show up as a ratio in the exponent of the Boltzmann factor, so that a fractional error in the DFT barrier is equivalent to a factional error in the inverse ripening temperature. The errors in DFT calculations are hard to estimate, but Giordano et al. have shown that different DFT functionals give rise to differences in binding energies on the order of 0.1 eV for this system [20]. The simulations indicate a ripening mechanism with a barrier of 1.4 eV, which leads to ripening temperature of 560 K. If we assume that this barrier has an uncertainty of ±0.1 eV, the corresponding range of ripening temperatures is between 520 and 600 K, which is comparable to the separation between experimental data points.

3.5. Charged defects

A possible reason that the KMC simulations based on DFT energetics show a lower ripening temperature (~400 K) than observed (~600 K) is that the F-center defect is not the one present in the experiment. The DFT calculations that were used as a basis for the KMC simulations shown in Fig. 7 assumed neutral oxygen vacancy defects, but it has been suggested that the important defects might be charged F^+-center oxygen vacancies or divacancies [20,27]. To test this possibility, we have re-calculated the binding energies of small clusters at charged F^+-center defects using DFT, and estimated the cluster dissociation barriers in our KMC model (see Table 2). For each dissociation mechanism, the binding energy is calcu-

Table 2
DFT-based kinetic parameters for small Pd$_n$ ($n = 1$–5) clusters bound at positively charged oxygen vacancies (F^+-centers)

Event (see Fig. 6)	E_B (eV)	Barrier (eV)
2(f) Dimer dissociation	1.16	1.37
3(e) Trimer dissociation (1)	1.59	2.02[a]
3(f) Trimer dissociation (2)	0.94	1.29[a]
4(c) Tetramer dissociation (1)	1.91	2.38[a]
4(d) Tetramer dissociation (2)	1.35	1.69[a]
5(b) Pentamer dissociation (1)	1.44	1.85[a]
5(c) Pentamer dissociation (2)	1.25	1.59[a]

Trimers, tetramers and pentamers dissociate from F^+-centers either by (1) detaching a cluster with one fewer atom and leaving a monomer behind on the defect, or by (2) detaching a monomer, leaving behind the smaller (Pd$_{n-1}$) cluster bound to the defect. The DFT calculation parameters are the same as the calculations on F-centers except that the total number of electrons in the system was reduced by one.
[a] Estimated from the binding energy plus the diffusion barrier of the dissociated species on the terrace.

lated as the difference between the initial and final states (see Fig. 6). For all clusters larger than the dimer, the dissociation barrier is taken as the sum of the binding energy and the diffusion barrier of the dissociating species on the terrace. This approximation ensures detailed balance in our KMC simulation.

The Pd monomer binds less strongly at the F^+-center (2.77 eV) as compared to the F-center (4.00 eV). This is consistent with a Bader charge density analysis, showing that Pd accepts charge from the surface [29]. With one fewer electron in the vacancy, the binding energy is reduced. This weaker bond to the surface, however, means that the Pd adatom can make stronger bonds to other Pd atoms on the surface. Table 2 shows that the dissociation mechanisms which leave behind a monomer-defect complex have a higher barrier at the charged vacancy than at the neutral one. The dimer binding energy, in particular, is significantly increased from 0.57 eV at the F-center to 1.16 eV
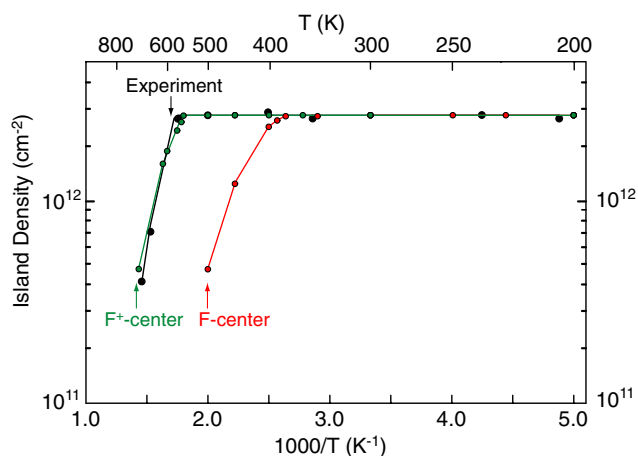

Fig. 9. Comparison of Pd island densities calculated with KMC using kinetic parameters based on DFT calculations of Pd clusters bound at F-center and charged F^+-center defects. The dynamics at F^+-center are in agreement with experiment, showing the same ripening temperature.

at the F^+-center. The corresponding increase in the dimer dissociation barrier from 0.70 eV to 1.37 eV dramatically changes the ripening temperature. Another interesting aspect of these calculations is that the trimer dissociation barrier is slightly lower than the dimer dissociation barrier at the F^+-center.

The Pd island density obtained from KMC simulations with parameters derived from these DFT results is shown in Fig. 9. The increased dissociation barrier of clusters at F^+-centers brings the simulations into agreement with experiment. This is largely due to the increase in the dimer dissociation barrier. The defect-bound dimer is even more stable than trimer so that at the 560 K ripening temperature observed in our KMC simulation, there are twice as many trimer dissociation events (441) as dimer dissociation events (215).

We note that Venables et al. [27] have recently reported rate equation calculations where the energetics were chosen to be consistent with the DFT calculations of cluster binding to F^+-centers [27].

4. Discussion

This work addresses two different aspects of modeling metal particle growth and sintering on oxides. First, there is the issue of determining the set of transitions which control Pd island growth and ripening (the model), and then there is the issue of how well a comparison of calculated results based on an assumed model with experimental data can be used to determine this set of transitions.

The kinetic model that we have built using results of DFT calculations combines phenomena that have been discussed in the recent literature. These include mobility of small clusters [30,46,22,23] and the nature of defects which determine the binding of clusters and the onset temperature of ripening [20,32,21,27]. Simulations of Pd island formation allow us to combine these microscopic mechanisms and observe which are important for the resulting kinetics. The simulations are far from equilibrium, so it is hard to predict a priori how significant a particular mechanism might be. For example, cluster mobility is observed to be important at temperatures near 200 K. Cluster mobility can also play a role in high temperature ripening because it allows for the dissociation of clusters of two or more atoms from large, immobile islands. This was not found to be so important in the Pd/MgO system, but it could be for other metal/oxide systems, or for other defects such as the divacancy [21,27].

A second consideration is how to evaluate whether a kinetic model captures the correct physics underlying observed phenomena. This is a non-trivial issue that goes beyond comparing a simulated Pd island density with what is observed experimentally. One should consider how many independent data points are being modeled, how many fitting parameters are in the model, and how many other possible models could be constructed which also agree with the experimental data. In this case, there are two dominant features in the Pd island density data: a constant density above 200 K and the onset of ripening at 600 K. With these limited data, models with more than one or two fitted parameters are likely non-unique. In the case of the rate equation based approach [17,25], a great deal of experience has been built into the model, but with two fitting parameters (the monomer diffusion and dimer dissociation rates) it would be surprising if the assumed model were unique.

The approach we have taken here is to derive all kinetic parameters (including diffusion mechanisms and energetics) from DFT calculations, and then determine whether the simulated island density matches experiment. If not, the assumptions in the DFT calculations should be questioned, such as the nature of defects in this case, or the approximations in DFT itself.

5. Conclusions

We have constructed a KMC model to simulate experimental measurements of Pd island growth on MgO(100) during Pd vapor deposition involving many atomic scale transitions that lead to diffusion, cluster nucleation and ripening. The KMC method is shown to be consistent with previous rate equation results, when compared using the same set of parameters. KMC simulations were then carried out including a variety of additional elementary steps that were neglected in earlier models, using parameters from DFT calculations, including small cluster diffusion, three-dimensional cluster formation, coalescence, and cluster breakup mechanisms. These simulations show that cluster mobility plays an important role for island growth at around 200 K, and that the onset temperature of ripening is directly related to the rate of dimer dissociation at defect sites. This ripening temperature is found to be lower than experiment, assuming neutral oxygen vacancy defects on the surface. When we assume charged vacancies, the island densities obtained from the KMC simulations are in agreement with experiment using directly energetics obtained from first principles DFT calculations and without any adjustment of parameters. As in the neutral vacancy case, the ripening temperature is determined by the rate of cluster dissociation at defects, but at the F^+-center, it is the trimer, rather than the dimer, which gives rise to the majority of ripening events. These DFT energetics, used with either KMC or rate equation based models [27], match experiment and provide detailed new insights regarding the mechanism of Pd diffusion during film growth and the nature of the defects on MgO(100) which influence Pd film growth.

References

[1] C.T. Campbell, Surf. Sci. Rep. 27 (1997) 1.
[2] C.R. Henry, Surf. Sci. Rep. 31 (1998) 235.
[3] J.A. Venables, Introduction to Surface and Thin Film Processes, Cambridge University Press, Cambridge, 2000.
[4] H.J. Freund, M. Bäumer, H. Kuhlenbeck, Adv. Catal. 45 (2000) 333.
[5] M. Moseler, H. Hakkinen, U. Landman, Phys. Rev. Lett. 89 (2002) 176103-1.
[6] T.H. Lee, R.M. Dickson, Proc. Natl. Acad. Sci. USA 100 (2003) 3043.
[7] P. Wynblatt, N.A. Gjostein, Progress in Solid State Chemistry, vol. 9, Elsevier Science, Amsterdam, 1975.
[8] G.B. Mcvicker, R.L. Garten, R. Baker, J. Catal. 54 (1978) 129.
[9] E. Ruckenstein, D.B. Dadyburjor, Rev. Chem. Eng. 1 (1983) 251.
[10] C.H. Bartholomew, Stud. Surf. Sci. Catal. 111 (1997) 585.
[11] M.J.J. Jak, C. Konstapela, A. van Kreuningena, J. Chrosta, J. Verhoevena, J.W.M. Frenken, Surf. Sci. 474 (2001) 28.
[12] X. Lai, D.W. Goodman, J. Mol. Catal. A 162 (2000) 33.
[13] C.T. Campbell, S.C. Parker, D.E. Starr, Science 298 (2002) 811.
[14] J.H. Harding, A.M. Stoneham, J.A. Venables, Phys. Rev. B 57 (1998) 6715.
[15] H. Fornander, J. Birch, L. Hultman, L.G. Petersson, J.E. Sundgren, Appl. Phys. Letts 68 (1996) 2636.
[16] G. Renaud, A. Barbier, Surf. Sci. 435 (1999) 142.
[17] J.A. Venables, J.H. Harding, J. Cryst. Growth 211 (2000) 27.
[18] B. Hammer, Phys. Rev. Lett. 89 (2002) 016102-1.
[19] G. Renaud, R. Lazzari, C. Revenant, A. Barbier, M. Noblet, O. Ulrich, F. Leroy, J. Jupille, Y. Borensztein, C.R. Henry, J.P. Deville, F. Scheurer, J. Mane-Mane, O. Fruchart, Science 300 (2003) 1416.
[20] L. Giordano, C. Di Valentin, J. Goniakowski, G. Pacchioni, Phys. Rev. Lett. 92 (2004) 096105-1.
[21] L. Giordano, G. Pacchioni, Surf. Sci. 575 (2005) 197.
[22] L. Xu, G. Henkelman, C.T. Campbell, H. Jónsson, Phys. Rev. Lett. 95 (2005) 146103-1.
[23] G. Barcaro, A. Fortunelli, F. Nita, R. Ferrando, Phys. Rev. Lett. 95 (2005) 246103-1.
[24] H. Brune, Surf. Sci. Rep. 31 (1998) 121.
[25] G. Haas, A. Menck, H. Brune, J.V. Barth, J.A. Venables, K. Kern, Phys. Rev. B 61 (2000) 11105.
[26] C. Ratsch, J.A. Venables, J. Vac. Sci. Technol. 21 (2003) S96.
[27] J.A. Venables, L. Giordano, J.H. Harding, J. Phys.: Condens. Matter 18 (2006) S411.
[28] C. Barth, C.R. Henry, Phys. Rev. Lett. 91 (2003) 196102-1.
[29] L. Xu, G. Henkelman, C.T. Campbell, H. Jónsson, Surf. Sci. 600 (2006) 1351.
[30] J. Carrey, J.L. Maurice, F. Petroff, A. Vaurès, Phys. Rev. Lett. 86 (2001) 4600.
[31] G. Pacchioni, Chem. Phys. Phys. Chem. 4 (2003) 1041.
[32] L. Giordano, C. Di Valentin, G. Pacchioni, J. Goniakowski, Chem. Phys. 309 (2005) 41.
[33] D. Fuks, Y.F. Zhukovskii, E.A. Kotomin, D.E. Ellis, Surf. Sci. Lett. 600 (2006) L99.
[34] A. Bogicevic, D.R. Jennison, Surf. Sci. Lett. 515 (2002) L481.
[35] G. Henkelman, H. Jónsson, J. Chem. Phys. 111 (1999) 7010.
[36] H. Jónsson, Annu. Rev. Phys. Chem. 51 (2000) 623.
[37] R.A. Olsen, G.J. Kroes, G. Henkelman, A. Arnaldsson, H. Jónsson, J. Chem. Phys. 121 (2004) 9776.
[38] A. Heyden, A.T. Bell, F.J. Keil, J. Chem. Phys. 123 (2005) 224101-1.
[39] A.B. Bortz, M.H. Kalos, J.L. Lebowitz, J. Comput. Phys. 17 (1975) 10.
[40] D.T. Gillespie, J. Comp. Phys. 22 (1976) 403.
[41] G.H. Gilmer, Science 208 (1980) 335.
[42] A.F. Voter, Phys. Rev. B 34 (1986) 6819.
[43] K.A. Fichthorn, W.H. Weinberg, J. Chem. Phys. 95 (1991) 1090.
[44] H. Graoui, S. Giorgio, C.R. Henry, Surf. Sci. 417 (1998) 350.
[45] W. Vervisch, C. Mottet, J. Goniakowski, Phys. Rev. B 65 (2002) 245411-1.
[46] J. Carrey, J.L. Maurice, F. Petroff, A. Vaurès, Surf. Sci. 504 (2002) 75.